Hot Carrier Mobility Dynamics Unravel Competing Sub-ps Processes in Lead Halide Perovskites

Andrés Burgos-Caminal, Juan Manuel Moreno-Naranjo, Aurélien René Willauer, Arun Aby Paraecattil, Ahmad Ajdarzadeh, and Jacques-E. Moser *

Photochemical Dynamics Group, Institute of Chemical Sciences and Engineering, and Lausanne Centre for Ultrafast Science (LACUS), École Polytechnique Fédérale de Lausanne, 1015 Lausanne, Switzerland

* Corresponding author, email: je.moser@epfl.ch

Abstract

The mechanisms behind the large photocarrier diffusion length and the outstanding photovoltaic performances of lead halide perovskites (LHP) are still debated. Hot carrier cooling and the formation of polarons are central to the charge separation process. Ultrabroadband terahertz spectroscopy with a time resolution <200 fs is applied to probe the early carrier mobility dynamics in LHP samples composed of various anions and cations. The increase of the mobility observed in the sub-ps timescale evidences the competition between carrier cooling and a dynamic screening process associated with polaron formation. The dependence of the mobility dynamics on the initial photocarrier density and excess excitation energy shows that carrier cooling is not only subjected to a phonon bottleneck but also competes with the dynamic screening effect. A kinetic model is established that successfully unifies the two previously proposed mechanisms. Simulations based on this evidence a chemical composition dependence of the dynamic screening lifetime.

Introduction

Lead halide perovskites (LHPs) have attracted much attention in recent years due to the outstanding photovoltaic performances of thin film solar cells based on these materials combined with their facile processability.[1,2] These advantages have encouraged many groups to seek a detailed understanding of the charge carrier and quasiparticle dynamics that govern the observed performances. Two of the main factors behind the large power conversion efficiencies are generally agreed to be a) slow recombination of photogenerated charge carriers [3] and b) a relatively large carrier mobility.[4] In combination, these two properties give rise to long diffusion lengths extending over micrometres [5] and consequently allow for efficient charge extraction in submicron thin films.

The recombination rates in LHPs are, indeed, up to 5 orders of magnitude slower than those predicted from Langevin theory for a direct bandgap semiconductor.[6] The reason behind this property is still an active topic of debate. One possibility that is gaining acceptance is that the carriers have a polaronic nature.[7] The polar character of the lattice screens the Coulomb potential of photogenerated charges, which then experience reduced scattering with other charges and lattice defects.[7,8] This effect should slow down not only recombination but also charge carrier cooling in comparison to bare charges.[9] Because of two counteracting phenomena, predicting whether the polaron formation produces an increase or a decrease in the observed carrier mobility is difficult. On the one hand, the lattice deformation associated with the polaron should produce a heavier effective mass. On the other hand, the dynamic screening of the Coulomb potential upon the formation of a large polaron will hinder the scattering of charges with lattice defects.[7] Meanwhile, hot carriers can undergo additional carrier-carrier scattering at high temperature and density, which can be screened upon polaron formation.[9] Therefore, time-resolved mobility measurements, such as those obtained through optical pump-THz probe spectroscopy, can be a useful way of detecting and defining the effects of polaron formation and scrutinizing the hot carrier dynamics. Several spectroscopic studies of hot photocarriers have recently been reported [10–15] along with theoretical studies focusing on the slow rate of this cooling.[16,17] The time evolution of hot carriers is of particular interest in view of the possibility of realizing photovoltaic cells with conversion efficiencies exceeding the Shockley-Queisser limit. Indeed, several studies have reported long hot carrier lifetimes up to tens of picoseconds, opening the way to extracting them at selective contacts.[18]

When studying early charge carrier dynamics, a good time resolution is essential to reach meaningful conclusions with the application of mathematical models. This time resolution can be achieved in time-resolved terahertz spectroscopy (TRTS) using an ultrabroadband THz single-cycle pulse generated with a two-colour plasma technique.[18] In our case, such a pulse includes frequencies from 1 to 20 THz,

allowing for a pulse duration as short as 200 fs instead of the ~1 ps pulse typically obtained by optical rectification in solid semiconductors (see the THz spectrum and pulse shape in the Supporting Information, SI Fig. S3). This can help to overcome the artefacts that may appear in classical TRTS on the sub-ps dynamics.[19] The use of ultrabroadband pulses poses, however, the difficulty of finding the right substrate with full transparency. Various approaches have been used in the past, such as employing Si wafers[20] and diamond as thin film substrates,[21] or using single-crystals in reflectance mode.[22,23] The latter substrates, however, either give rise to strongly modulated absorption spectra and pose an excessive experimental and analytical complexity or are too costly. In addition, it is of interest to study the perovskite response in a state close to that of a working optoelectronic device. Thus, we measured polycrystalline thin films in a transmission configuration. To address this problem, we developed a simple method to deposit LHP thin films on plastic sheets, such as high-density polyethylene (HDPE), fully transparent to our 1-20 THz pulses. These samples do not appear to be affected by the substrate in their photophysics (see the absorption and emission spectra in SI, Fig. S1). In addition, the resulting films are polycrystalline with some grains being more than 100 nm long (SI, Fig. S2). Furthermore, all ultrafast measurements focus on the first ps, before surface recombination becomes really important.

Methods

Sample preparation – Thin film samples were prepared by spin-coating using an antisolvent method [24] on fully THz transparent HDPE substrates (1 × 15 × 15 mm). The substrates were cleaned using a sonicating bath in a Hellmanex® solution and subsequently rinsed with ultrapure water, acetone, ethanol and high purity methanol. Directly afterward, the substrates were submitted to an oxidative plasma treatment for 90 min. This treatment allowed a better wettability of the apolar polymer with polar solutions through the creation of oxidized polar groups on the surface. Precursor solutions (1 mmol in 1 mL of DMSO) were prepared for deposition. In the case of $CsPbIBr_3$, due to the low solubility, the saturated solution of the mentioned mixture was used. Spin-coating was carried out as follows: a sufficient amount of solution was extended over the substrate. The sample was spun at 1000 rpm for 10 s and subsequently at 6000 rpm for 30 s. Ten seconds before the end, 200 µL of chlorobenzene was poured onto the spinning substrate to act as an antisolvent and improve crystallization. Last, the sample was annealed at 100 °C to obtain a perovskite layer of the characteristic colour (see spectral characterizations of the films in SI, Fig. S1).

Ultrabroadband time-resolved THz spectroscopy – TRTS measurements were carried out on a previously described laser spectrometer,[25,26] with a few modifications. Three beams were split from the fundamental output (45 fs pulse duration, λ = 800 nm, 1 kHz repetition rate) of an amplified

Ti:sapphire laser (Libra, Coherent) and used for the TRTS experiments. The first beam was employed to pump a white light-seeded optical parametric amplifier (OPerA Solo, Coherent) that provided the pump pulses for the pump–probe experiment at tuneable wavelengths. Alternatively, the same beam could be diverted to obtain 400 nm pulses through second harmonic generation in a BBO crystal. The more powerful of the two remaining beams (390 µJ per pulse) was used to generate the probe beam, consisting of a train of short and broadband THz pulses, through a two-colour plasma method:[27] The beam was focused with a fused silica lens (f = 75 mm), and the second harmonic was generated with a 100 µm BBO crystal. At the focal point, the electric field of the two-colour beam was sufficiently strong to form a plasma filament in nitrogen that radiated a broadband THz pulse (200 fs, 1–20 THz) that was subsequently collimated and focused with parabolic gold mirrors onto the sample. To maximize THz generation, a dual wavelength waveplate was used immediately after the BBO crystal to obtain fundamental and second harmonic beams of equal polarization after type 1 phase matching.[28] The transmitted beam went through two additional parabolic mirrors towards a homemade ABCD (air-biased coherent detection) detector.[29] Silicon wafers were used to filter the visible light from the THz generation and pumping. The remaining beam (40 µJ/pulse) was used as a gate for the detection, generating a second harmonic signal proportional to the THz electric field measured with a PMT (PMM01, Thorlabs). The SHG process was carried out in an enclosed box with TPX® windows, where the atmosphere can be replaced with butane gas.[30] This setup allowed an increase in the sensitivity at the expense of frequencies in the 12-20 THz range. It was used to increase the signal-to-noise ratio in the frequency-averaged dynamics.

Calculations – The data were fitted to the model using Wolfram *Mathematica* software. The differential equations were written following the model depicted in Scheme 2 and numerically solved for an interval covering the data. The signal was simulated as a normalized and weighted sum of the different carrier densities with the condition that it equals zero for times earlier than t_0. The result was numerically convoluted with a Gaussian function to account for the IRF. An interpolation function was fitted to the results to calculate the value at any times inside the calculated interval. A short time step of 0.005 fs was used for the calculation, which was shown to be sufficient to obtain results identical to those with simpler functions for which an analytical solution is possible.

Results and Discussion

We aim to study the relationship between carrier-lattice interactions and carrier cooling from a mobility perspective using TRTS. Such a study can be achieved by exploiting the sensitivity of THz radiation transmission to the carrier mobility. In an optical pump-THz probe experiment applied to a semiconductor material, the pump generates charge carriers that absorb the incident THz probe pulse.

The THz radiation absorptance is generally reported as the negative of the ratio between the change in the modulus of the THz electric field (ΔE) upon transmission through the sample and the modulus of the incident field (E). In the case of thin films, when $\Delta E << E$, this ratio can be shown to be proportional to the photoconductivity ($\Delta\sigma$) generated by the photogenerated carriers, which is itself proportional to the carrier density (N) and the carrier mobility (μ) (Eq. 1).[31,32]

$$\frac{-\Delta E}{E} \propto \Delta\sigma = \mu \cdot \mathrm{e} \cdot N \quad (1)$$

An evolution of the THz absorptance of the sample must therefore be associated with a change in either N or μ. With this in mind, we determined the early carrier dynamics of three LHP thin films of various compositions, namely, $CH_3NH_3PbI_3$, $CH_3NH_3PbBr_3$, and $CsPbBr_3$, using ultrabroadband TRTS. Fig. 1 shows the charge carrier photoconductivity dynamics measured during the first picoseconds following photoexcitation at different pump wavelengths of a $CH_3NH_3PbI_3$ thin film deposited on HDPE. At resonant photon energies, a fast rise can be observed while, above resonant energies, a second slower rise becomes increasingly apparent with increasing excitation energy.

It is worth noting that these measurements were carried out focusing on the point of highest electric field of the THz pulse. This approach is valid if the $\Delta E(t)$ waveform is not phase-shifted with respect to the initial pulse. In order to verify this point, we obtained a 2D map of the different $\Delta E(t)$ waveforms and the corresponding $-\Delta E(\omega)/E(\omega)$ spectra. As seen in SI, Figs. S4 and S5, the slower rise is coming mainly from a change in amplitude. However, the spectral response is not trivial and cannot generally be assigned to a simple model such as Drude or Drude-Smith.[33] Nonetheless, the response rises quite uniformly on the 5 to 12 THz range, where most of the THz probe is located. Thus, we can use the frequency averaged response following the maximum at $t = 0$ (SI, Fig. S4 A) as a general probe of the photoconductivity evolution. This allows us to carry out measurements in many different conditions of pump wavelength and fluence without the need to obtain costly 2D maps.

Returning to the results in Fig. 1, in terms of Eq. 1, the fast initial rise can be assigned to an increase in the carrier density N upon photoexcitation, mixed with the initial steps of carrier evolution such as thermalization,[34] coherence loss,[35] the development of many body interactions,[21] and, perhaps, the initial steps of carrier cooling. Although the time resolution of our setup can be expected to be shorter than this rise we are unable to distinguish between the different processes. In addition, this rise can be well fitted to the convolution of an instantaneous rise with a Gaussian having a FWHM of 200 fs (See SI, Fig. S6). Therefore, hereon the data will be treated as having a time resolution limit of 200 fs. On the other hand, the latter rise cannot be assigned to a further rise in N, as there is no more source of free carriers. Slow exciton dissociation would be more important at resonant conditions and not at

above bandgap excitation, where carriers are quickly generated. Instead the latter rise can be more easily related to hot carrier evolution affecting the mobility μ. Such behaviour of the mobility has been previously reported, e.g., for GaAs [36] or perovskites,[12,37] and is generally associated with the formation of hot charge carriers at different positions of the band structure $U_E(\boldsymbol{k})$ away from the bandgap threshold (Scheme 1). This behaviour is due to the relation between the mobility, effective mass and band curvature. Indeed, the mobility μ inversely depends on the effective mass m^*, while m^* in turn inversely depends on the band curvature ρ.[38] In a simplified one-dimensional approximation, the carrier mobility μ is then proportional to the band curvature ρ and the scattering time τ_s (Eq. 2).

$$\mu = \mathrm{e} \cdot \tau_s \cdot \frac{1}{m^*} = \mathrm{e} \cdot \tau_s \cdot \frac{1}{\hbar^2} \cdot \frac{\partial^2 U_E}{\partial k_j^{\,2}} = \frac{e}{\hbar^2} \cdot \tau_s \cdot \rho \qquad (2)$$

Scheme 1 displays a simplified band structure of $CH_3NH_3PbI_3$, where the spin-orbit coupling has been omitted for the sake of simplification.[39] In such a situation, carriers photogenerated upon excitation in the blue region experience a significantly lower curvature of both the conduction and valence bands (positions A and A'). Hence, they must be characterized by a larger effective mass (m^*) and a lower mobility (μ) compared to carriers photogenerated upon excitation in the red region (positions B and B'). In addition, calculations suggest that a loss of parabolicity occurs as close as one-third from the minimum point along any direction (Scheme 1).[39] This loss produces a decrease in mobility for the carriers higher up in the valley.[40,41] Thus, relatively small excess energies already produce a noticeable decrease in the initial average mobility μ, even though no carriers are located in different valleys.

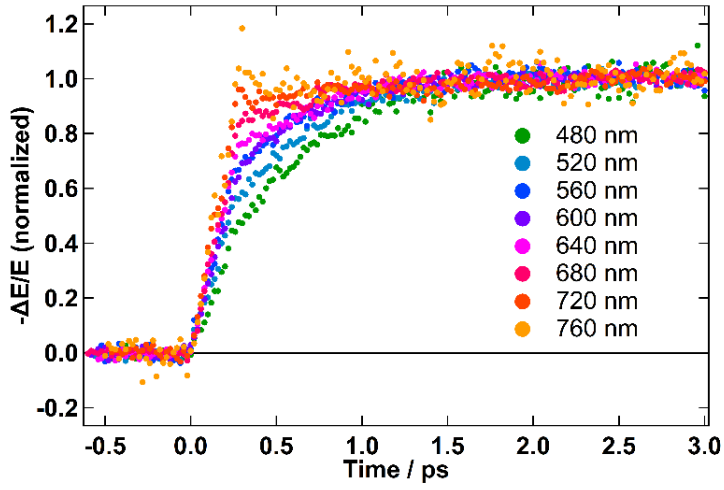

Figure 1. Excitation wavelength dependence of the early photoconductivity dynamics in $CH_3NH_3PbI_3$ thin films as probed by ultrabroadband TRTS for carrier densities above 10^{18} cm^{-3}, similar for all traces. The terahertz absorptance $-\Delta E/E$ is directly proportional to the photoconductivity $\Delta\sigma$.

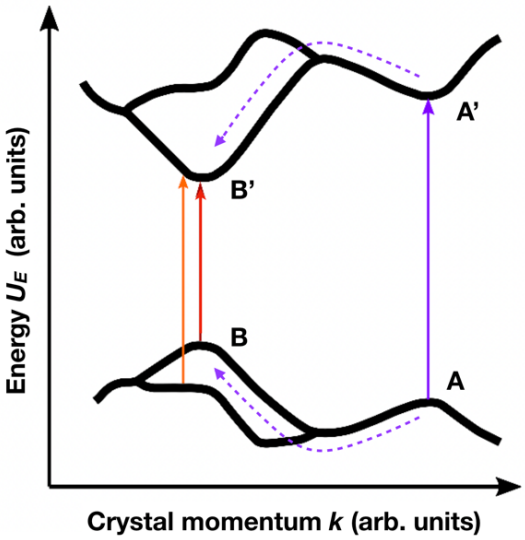

Scheme 1. Simplified band structure scheme based on ref. [39]. Direct transitions occurring at λ_{ex} = 800 nm (red), λ_{ex} = 600 nm (orange) and λ_{ex} = 400 nm (purple) are represented by vertical arrows. The dashed arrows represent a cooling pathway of photocarriers generated upon excitation at λ_{ex} = 400 nm.

Then, from a simple perspective, the observation of the slower rise in the THz absorptance over time can initially be assigned to intravalley relaxation and intervalley scattering of hot carriers with phonons towards the bottom of the valley where the effective mass accounts for the maximum mobility. In order to model such a process, we first consider a simple situation with low mobility hot carrier (N_H) and high mobility cold carrier (N_C) populations. This simplified model (see details in SI, section S3a) gives rise to a single exponential time profile of the transient photoconductivity signal (Eq. 3):

$$S(t) = 1 - B \cdot \exp\left(-\frac{t}{\tau}\right) \tag{3}$$

where B is the amplitude and τ is the lifetime. In such a simplified model, carriers can only be either hot or cold. However, a distribution of carriers with different excess energies and, thus, mobilities characterized by a certain temperature exists in reality. In addition, one should consider the possibility of polaron formation. Despite its limitation, fitting this initial simple model can be useful in evaluating the lifetime of the process involved. Parameter *B* in Eq. 3 is a measure of the difference in average mobility of the ensemble between the initial and final situations (see further explanation in the SI, section S3a). A convolution with a Gaussian of FWHM *w* accounting for the instrument response function (IRF) can be used to fit the data (see SI, Eqs. S7, S8). The results of the data fitting shown in Fig. 1, with different measurements at different pump wavelengths (λ), are found in Table 1. Due to the initial rise previously explained, the value of the FWHM *w* is also fitted. We repeatedly obtain values of *ca.* 200 fs.

Table 1. Results for the fitting of the simple exponential model (see SI, Eq. S8) at different pump wavelengths (λ_{exc}) for $CH_3NH_3PbI_3$. The fitting curves are shown in the SI (Fig. S7).

λ_{exc} / nm	*B* / -	τ / ps	*w* / ps
480	0.78 ± 0.05	0.50 ± 0.02	0.17 ± 0.04
520	0.63 ± 0.02	0.46 ± 0.01	0.20 ± 0.01
560	0.51 ± 0.03	0.39 ± 0.02	0.18 ± 0.01
600	0.48 ± 0.02	0.41 ± 0.01	0.22 ± 0.01
640	0.38 ± 0.02	0.44 ± 0.02	0.19 ± 0.01
680	0.22 ± 0.02	0.45 ± 0.03	0.21 ± 0.01

As expected, the amplitude *B* increases with excess energy owing to the higher initial concentration of hot carriers. Surprisingly, however, the lifetimes from the measurements are fairly constant in the 480-680 nm excitation wavelength range, with values between 400 and 500 fs. Above 680 nm, the rise is almost negligible. The lack of an increase in the lifetime is surprising if we assign it to carrier cooling, as the higher the initial carrier temperature is, the longer cooling down should generally take.[13] If the THz absorption is a direct probe of the average carrier temperature, then this would indeed be the case. However, the exponential fits with a constant lifetime indicate a different process that links high and low mobility carriers. The relaxation of hot charge carriers includes two initial steps: a) thermalization, in which the hot carriers equilibrate towards a Fermi-Dirac distribution, characterized by a certain temperature higher than that of the lattice, and b) cooling, in which the hot carriers interact with the lattice through carrier-phonon inelastic scattering with longitudinal optical (LO) phonons to shed their extra energy.[18] The former step has been reported to occur in the 10 to 100 fs interval,[34] below the initial rise, while the latter step can actually be studied with TRTS. LO phonons are considered to be involved not only in the relaxation of hot carriers [13] but also in polaron formation.[42] Recently, time-resolved spectroscopy techniques other than TRTS have revealed that the polaron formation time for LHPs is on the order of hundreds of fs.[42] As a type of carrier-phonon coupling, the appearance of polarons should be kinetically determined by the emergence of phonon-carrier interactions. In ref. [42], the perovskites under study were $CH_3NH_3PbBr_3$ and $CsPbBr_3$. For these materials, we obtained, on average, low mobility lifetimes of 320 and 650 fs, very close to the reported polaron formation times of 290 and 700 fs, respectively. Note that these lifetimes are subject to a certain variability depending on the sample. Interestingly, for some of the measurements reported in the literature, the observed process did not involve any cooling since a resonant excitation was used.

A recent publication reported a direct observation of polaron formation with TRTS.[12] Surprisingly, the authors observe a delayed rise of the photoconductivity, which is assigned to polaron formation. A rise that we do not observe on the frequency averaged photoconductivity at resonant conditions. It is unclear whether this comes from a delayed response at lower frequencies or due to a lower time resolution in optical rectification based TRTS setups. From our 2D maps it does seem that a delayed rise can be observed at frequencies lower than 2.5 THz (see SI, Fig. S8) and it coincidently is of the same order as the reported polaron formation times. Furthermore, broadband TRTS based on gas photonics has recently been used to investigate the early dynamics on single-crystal $CH_3NH_3PbI_3$ samples in reflectivity mode upon resonant pumping.[23] In the latter study, a coherent oscillation is reported in the pump-probe dynamics mixed with a rise in the photoconductivity. It was also observed that this rise becomes longer at lower frequencies. Interestingly, a deeper analysis of the probe frequency dependence of the oscillations allows to relate both phenomena to the formation of polarons. Such polaron formation is found to originate from the coupling to a single LO phonon mode at 3.7 THz. Unfortunately, we are unable to observe such clear oscillations and their dependency on probe frequency. This can be explained by the apparent lower sensitivity of our setup and the nature of our samples. Single crystals with a fixed orientation might enhance these kind of responses. Nonetheless, there is a change in the photoconductivity spectrum occurring in the first hundreds of femtoseconds (see SI, Fig. S9). We may tentatively assign it to the formation of polarons because, from a Drude perspective, a change only in effective mass should only change the amplitude of the spectrum. In fact, the very early spectra are the only ones that show the characteristic shape of the Drude-Smith model (Figure S10) for free carriers in a nanocrystalline solid. On the other hand, the final spectrum shows a photoconductivity that rises for frequencies higher than *ca.* 3.7 THz. This may be caused by a different absorption of the THz waves above and below the coupled phonon frequency.[23] A further in-depth study of the photoconductivity spectrum is beyond the scope of this paper and will be conducted in the future. More evidence of polaron formation in TRTS was obtained by Cinquanta *et al.* by looking at the phonon modes below 2 THz on $CsPbBr_3$ nanocrystals.[43]

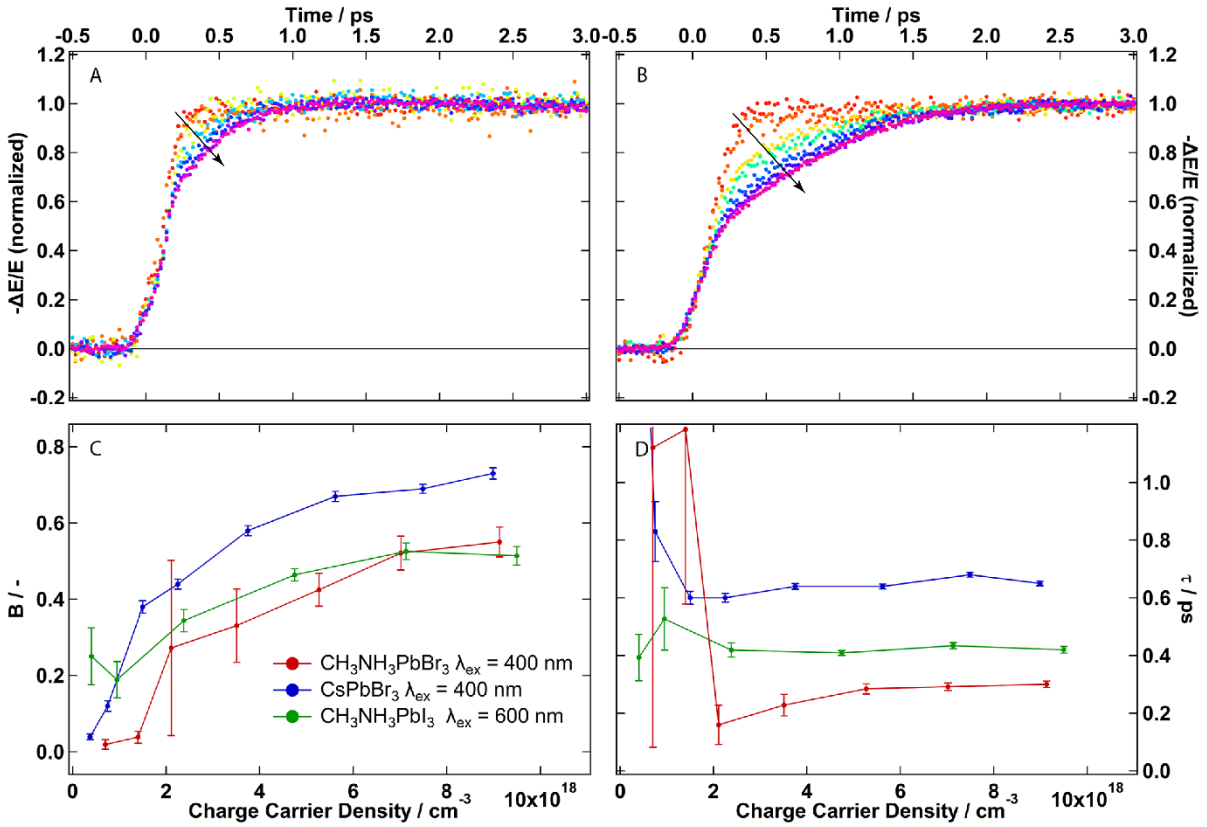

Figure 2. Fluence dependence of the rise in photoconductivity for A) $CH_3NH_3PbBr_3$ and B) $CsPbBr_3$. Note that both materials present a similar fluence dependence, while the lifetime is noticeably longer in the fully inorganic material. The arrows indicate the rise in fluence. C) The amplitude *B* from the fit is shown to be the main parameter that varies with fluence, while D) the time constant τ saturates earlier. A similar behaviour is found for $CH_3NH_3PbI_3$, as seen in C) and D). The fitting curves are shown in the SI, Fig. S7.

From the existing experimental evidence, polaron formation in the form of a dynamic screening process has been suggested to be in competition with carrier cooling.[9] Indeed, this dynamic screening process could result in polaron formation with the observed lifetimes. In Fig. 1, we show measurements for relatively high charge carrier densities, above 10^{18} cm^{-3}. At these densities, a slow cooling process is expected to be observed due to the phonon bottleneck typically observed in these materials.[44] Thus, if two competing processes occur, we can hypothesize that, at low densities, carrier cooling to the lattice temperature is sufficiently fast to occur before polaron formation, while at higher densities, the opposite is true. To test this hypothesis, we perform fluence-dependent measurements, as shown in Fig. 2.

Indeed, the data show an increase in the magnitude of the mobility rise with increasing fluence. Our data shows, nonetheless, that the formation of polarons does not produce a substantially large change in mobility if the carriers are already cold. When exciting the samples at resonant energies or at low

fluences, the slower rise is not observed (Figs. 1, 2 and SI, Fig. S11). Thus, the frequency averaged photoconductivity remains similar, while the spectrum suffers some change as previously mentioned. This result is intriguing because polaron formation should have mobility changes associated with it due to a) an increase in the effective mass while carrying the lattice deformation (lower mobility) and b) a decrease in scattering with defects (higher mobility).[7] These effects may compensate each other for cold carriers, leaving only a minor spectrum change that cancels out in the frequency averaged dynamics. Moreover, the fact that a rise with the polaron formation lifetime is observed at high fluences over the bandgap indicates that the dynamic screening process does produce a substantial increase in the hot carrier mobility. The dynamic screening may possibly reduce the carrier-carrier scattering present at high carrier temperatures. Thus, the mobility would increase upon hot polaron formation, unlike with cold polaron formation. Furthermore, the hot polarons present a much slower cooling, which prevents us from observing any further dynamics due to the strong Coulomb screening of the lattice.[9,45,46] We can thus propose the model depicted in Scheme 2.

According to this model, hot carriers turn into cold ones through phonon emission (k_1). This step is considered reversible (k_{-1}), introducing a hot phonon bottleneck. The phonons decay at a certain rate (k_3) such that a phonon population builds up at high hot carrier densities, decreasing the overall rate of carrier cooling. Indeed, these two processes imply that at low initial densities all carriers quickly cool down in under 200 fs (See the lowest fluence in Figure 2). On the contrary, at high densities the process is halted when an equilibrium is reached and proceeds much more slowly thereafter. This cooling process competes with the polaron formation process through dynamic screening (k_2), which has a certain lifetime depending on the perovskite composition. As the initial hot carrier density increases, the cooling process is slowed and hot polaron formation is favoured, giving rise to very long hot (polaronic) carrier lifetimes. From our observations, we ascribe the strong increase in mobility to bare carrier cooling and hot polaron formation. We consider that polaron formation is an irreversible process. Indeed, while theoretical calculations estimate the stabilization energy at around 50 meV,[47] twice the thermal energy at room temperature (25 meV), several clues point towards an effectively irreversible process of formation: a) The polaron formation process shows a characteristic lifetime both in our study and in others,[12,42] contrary to the greater variability with fluence that an equilibrium would show, and b) Polaron formation has drastic effects in the recombination of carriers, substantially increasing recombination times. If there was an equilibrium between free unscreened carriers and polarons, these would quickly recombine via the former. In summary, from this model, we can assign two different rises: a quick rise where fast cooling occurs before the equilibrium bottleneck and a slow rise where cooling is mixed with polaron formation. The relative magnitude between the two rises depends on the initial hot carrier density. The mobility change apparently stops once all carriers are in

the form of polarons, since cooling becomes very slow (k_4). Otherwise, if carrier cooling subjected to a phonon bottleneck were the only active mechanism, the second photoconductivity rise would become even slower as the excitation density increases. Once again, we use a simplified model that does not consider carrier and phonon energy distributions with a certain temperature. Nonetheless, this model appreciably follows the excitation fluence and wavelength dependencies that we observe. We justify not using a temperature model [13] by the fact that the function relating temperature and mobility is difficult to obtain and we can hardly assume that it is linear. Moreover, using such a model would overcomplicate the computation.

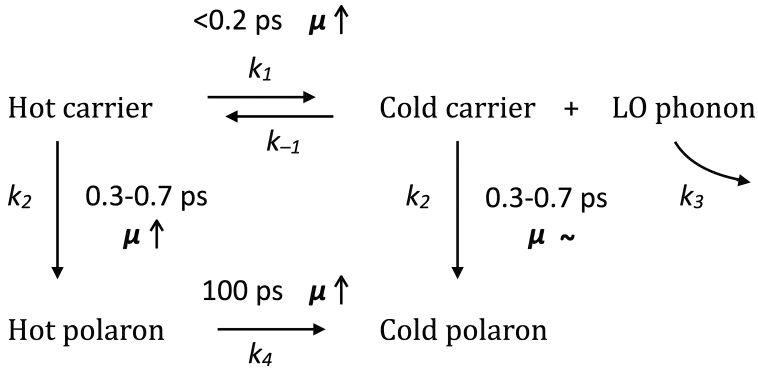

Scheme 2. Cooling and dynamic screening competition model. The different processes induce a change in the mobility in the direction represented by the arrows next to μ. The carrier cooling and hot polaron formation processes induce a stronger increase in the mobility in the time window analysed herein. LO phonons should also be produced upon polaron cooling. However, since this process occurs at longer times than the observed window the model is simplified by ignoring this fact.

As shown in Fig. 3, we can numerically solve the differential equations in the model in order to simulate the signal at different carrier densities (see details in SI, Section S3 b). These results show the same trends as the measurements in Fig. 2A. Furthermore, a global fitting of several datasets can be carried out in which all the parameters are common except for the initial charge carrier concentration, which can be fixed to a value proportional to the relative fluence used. The good quality of the fits supports the general validity of the model. While it has a similar shape to the exponential model, the competition model follows and explains the observed trend with fluence. Unfortunately, the complexity of the model prevents meaningful values from being obtained for each parameter in free fits, and many of the parameters have to be prefixed and guessed. Nonetheless, the importance lies in the general behavior and trends with fluence and wavelength that arise from the competing cooling and dynamic screening processes. The results of the fitting procedure are shown in Table 2. We obtain a time constant for polaron formation $1/k_2$ = 0.4 ps. Large values of the kinetic constants k_1 and k_{-1}

are guessed, since the equilibrium between hot carriers, on the one hand, and cold carriers and LO phonons, on the other hand, (Scheme 2) must be reached within the initial rise. The rate constants for phonon decay (k_3) and polaron cooling (k_4) are taken from the literature.[9,13] The fitted value of the parameter a = 0 (SI, Eq. S14) means that hot carriers do not contribute to the transient conductivity signal. The results for $CsPbBr_3$ are shown in the SI, Table S1 and Fig. S12.

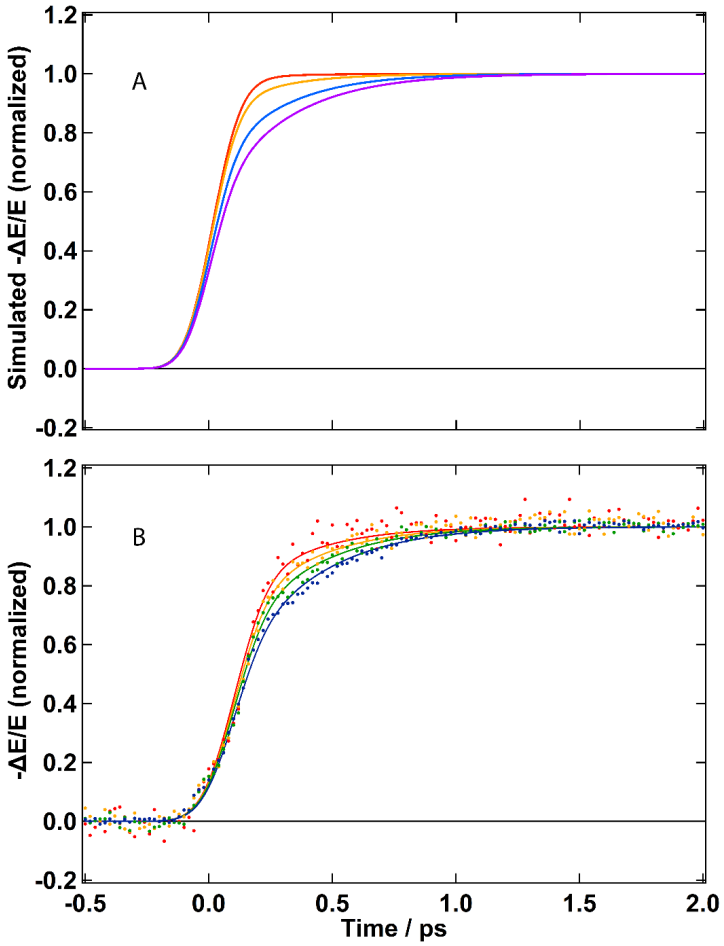

Figure 3. A) Simulated signals for $CH_3NH_3PbBr_3$ at different charge carrier densities following the model of Scheme 2 (see details in SI, section S3b). The slower rise becomes more apparent as the density is increased. B) Model global fittings to $CH_3NH_3PbBr_3$ data at 18 μJ/cm^2 (red), 31 μJ/cm^2 (yellow), 46 μJ/cm^2 (green), and 80 μJ/cm^2 (blue), where all parameters are common and the initial carrier density is proportional to the fluence multiplied by a common fitted value.

Our results, observing the previously reported polaron formation times [42] at higher fluences (<10^{18} cm^{-3}), come into contrast with the idea that polarons are destabilized at photocarrier densities higher than the Mott limit (~10^{18}cm^{-3}) due to mutual interaction.[9] The fact that we still observe the characteristic lifetime indicates that the process is still taking place. The destabilization of the polarons may induce a reduced screening, increasing the cooling rate of hot polarons, as found by Zhu and co-

workers,[45] but without preventing their formation. Nonetheless, this cooling would still take place beyond our observed time window, involve the phonon bottleneck, and compete with recombination. This behaviour could be related to the recent observation of quasi-particles that persist above the Mott density in $CH_3NH_3PbBr_3$ in the form of Mahan excitons.[48]

Table 2. Results of the global fitting of the complex model to experimental data as seen in Fig. 3B for $CH_3NH_3PbBr_3$. The parameter *w* stands for the FWHM of the convoluted Gaussian, a measure of the time resolution of the setup. The initial hot carrier density $N_{hc}(0)$ is given in arbitrary density units (adu). The same units are used in the dimensions of the second order rate constant k_{-1}.

Parameter	*Fitted value*
a	0 ± 0.08
$N_{hc}(0)$	0.3 ± 0.07 adu
w	0.24 ± 0.005 ps
k_1	200 ps^{-1} (guessed)
k_{-1}	100 $adu^{-1}\,ps^{-1}$ (guessed)
$k_{-1} \cdot N_{hc}(0)$	30 ± 7 ps^{-1}
k_2	2.5 ± 0.15 ps^{-1}
k_3	1.67 ps^{-1} (literature)
k_4	0.01 ps^{-1} (literature)

Further information on the LHP materials can be extracted from a comparison between different compositions in terms of cations and anions. One key parameter is affected: the dynamic screening lifetime, upon which both anions and cations have an effect. $CsPbBr_3$ is the material presenting the longest one, suggesting that the extra degrees of freedom from the organic cations play a role in speeding up the process. Last, low temperature measurements show an increase in the lifetime of the mobility rise accompanied by an increase in the total terahertz absorption (see SI, Fig. S13). The latter phenomenon is known in LHPs, where the polaron mobility is limited by polaron-phonon scattering.[20] Thus, at lower temperatures, the mobility is higher due to the lower population of phonons. The former phenomenon indicates a role of the phonon density in the polaron formation process.

Conclusions

Hot carrier dynamics of LHPs of different chemical compositions have been analysed from a THz mobility perspective using ultra-broadband TRTS in transmission mode. This was achieved through the novel use of HDPE substrates treated with an oxidative plasma. The results are compatible with competing cooling and dynamic screening processes. A model was proposed and applied to explain the observed fluence dependence and constant lifetime of the mobility rise. In it, the previously reported phenomena of a phonon bottleneck and polaron formation through a dynamic screening process were unified. Particularly, polaron formation was found to produce a substantial change in mobility especially for hot carriers. Furthermore, the composition appears to mainly affect the time constant of the dynamic screening process. In this regard, the Cs^+ inorganic cation was found to produce longer dynamic screening than its organic counterparts for a given halide composition. This result is probably due to a decrease in the degrees of freedom that allow for polarization of the lattice in the presence of a charge carrier. Last, low temperature measurements hint at implications of the phonon densities in the dynamic screening process.

Acknowledgements

Financial support by the Swiss National Science Foundation (SNF, Grant No. 200021_175729) and the National Center of Competence in Research "Molecular Ultrafast Science and Technology" (NCCR-MUST), a research instrument of the SNF, is gratefully acknowledged. The authors also thank Linfeng Pan, EPF Lausanne, for his help with SEM measurements.

Supporting Information

Details on the selection of a suitable polymer substrate, the sample preparation and the optical characterization – Ultrabroadband THz pulse and spectrum characterization – Details of the mathematical models – Supplementary experimental data: a) Evolution of the photoconductivity spectra, b) Fit of the initial rise, c) Delayed rise at lower frequencies, d) Drude-Smith analysis of very early THz signals, e) Fluence dependence of the THz absorptance signal at resonant excitation for $CH_3NH_3PbBr_3$ and $CsPbBr_3$, and f) Low temperature measurements of the early dynamics of the THz absorptance in $CH_3NH_3PbBr_3$.

References

(1) Correa-Baena, J.-P.; Abate, A.; Saliba, M.; Tress, W.; Jacobsson, T. J.; Grätzel, M.; Hagfeldt, A. The Rapid Evolution of Highly Efficient Perovskite Solar Cells. *Energy Environ. Sci.* **2017**, *10*, 710–727.

(2) NREL. Photovoltaic Research Efficiency Chart https://www.nrel.gov/pv/cell-efficiency.html (accessed Nov. 20, 2020).

(3) Bi, Y.; Hutter, E. M.; Fang, Y.; Dong, Q.; Huang, J.; Savenije, T. J. Charge Carrier Lifetimes Exceeding 15 μs in Methylammonium Lead Iodide Single Crystals. *J. Phys. Chem. Lett.* **2016**, *7*, 923–928.

(4) Herz, L. M. Charge-Carrier Mobilities in Metal Halide Perovskites: Fundamental Mechanisms and Limits. *ACS Energy Lett.* **2017**, 1539–1548.

(5) Stranks, S. D.; Eperon, G. E.; Grancini, G.; Menelaou, C.; Alcocer, M. J. P.; Leijtens, T.; Herz, L. M.; Petrozza, A.; Snaith, H. J. Electron-Hole Diffusion Lengths Exceeding 1 Micrometer in an Organometal Trihalide Perovskite Absorber. *Science* **2013**, *342*, 341–344.

(6) Wehrenfennig, C.; Liu, M.; J. Snaith, H.; B. Johnston, M.; M. Herz, L. Charge-Carrier Dynamics in Vapour-Deposited Films of the Organolead Halide Perovskite $CH_3NH_3PbI_{3-x}Cl_x$. *Energy Environ. Sci.* **2014**, *7*, 2269–2275.

(7) Zhu, X.-Y.; Podzorov, V. Charge Carriers in Hybrid Organic–Inorganic Lead Halide Perovskites Might Be Protected as Large Polarons. *J. Phys. Chem. Lett.* **2015**, *6*, 4758–4761.

(8) Miyata, K.; Atallah, T. L.; Zhu, X.-Y. Lead Halide Perovskites: Crystal-Liquid Duality, Phonon Glass Electron Crystals, and Large Polaron Formation. *Sci. Adv.* **2017**, *3*, e1701469.

(9) Joshi, P. P.; Maehrlein, S. F.; Zhu, X. Dynamic Screening and Slow Cooling of Hot Carriers in Lead Halide Perovskites. *Adv. Mater.* **2019**, 1803054.

(10) Hedley, G. J.; Quarti, C.; Harwell, J.; Prezhdo, O. V.; Beljonne, D.; Samuel, I. D. W. Hot-Hole Cooling Controls the Initial Ultrafast Relaxation in Methylammonium Lead Iodide Perovskite. *Sci. Rep.* **2018**, *8*, 8115.

(11) Price, M. B.; Butkus, J.; Jellicoe, T. C.; Sadhanala, A.; Briane, A.; Halpert, J. E.; Broch, K.; Hodgkiss, J. M.; Friend, R. H.; Deschler, F. Hot-Carrier Cooling and Photoinduced Refractive Index Changes in Organic–Inorganic Lead Halide Perovskites. *Nat. Commun.* **2015**, *6*, 8420.

(12) Bretschneider, S. A.; Ivanov, I.; Wang, H. I.; Miyata, K.; Zhu, X.; Bonn, M. Quantifying Polaron Formation and Charge Carrier Cooling in Lead-Iodide Perovskites. *Adv. Mater.* **2018**, 1707312.

(13) Fu, J.; Xu, Q.; Han, G.; Wu, B.; Huan, C. H. A.; Leek, M. L.; Sum, T. C. Hot Carrier Cooling Mechanisms in Halide Perovskites. *Nat. Commun.* **2017**, *8*, 1300.

(14) Shen, Q.; Ripolles, T. S.; Even, J.; Ogomi, Y.; Nishinaka, K.; Izuishi, T.; Nakazawa, N.; Zhang, Y.; Ding, C.; Liu, F. et al. Slow Hot Carrier Cooling in Cesium Lead Iodide Perovskites. *Appl. Phys. Lett.* **2017**, *111*, 153903.

(15) Guo, Z.; Wan, Y.; Yang, M.; Snaider, J.; Zhu, K.; Huang, L. Long-Range Hot-Carrier Transport in Hybrid Perovskites Visualized by Ultrafast Microscopy. *Science* **2017**, *356*, 59–62.

(16) Frost, J. M.; Whalley, L. D.; Walsh, A. Slow Cooling of Hot Polarons in Halide Perovskite Solar Cells. *ACS Energy Lett.* **2017**, *2*, 2647–2652.

(17) Madjet, M. E.; Berdiyorov, G. R.; El-Mellouhi, F.; Alharbi, F. H.; Akimov, A. V.; Kais, S. Cation Effect on Hot Carrier Cooling in Halide Perovskite Materials. *J. Phys. Chem. Lett.* **2017**, *8*, 4439–4445.

(18) Li, M.; Fu, J.; Xu, Q.; Sum, T. C. Slow Hot-Carrier Cooling in Halide Perovskites: Prospects for Hot-Carrier Solar Cells. *Adv. Mater.* **2019**, *0*, 1802486.

(19) Nienhuys, H.-K.; Sundström, V. Intrinsic Complications in the Analysis of Optical-Pump, Terahertz Probe Experiments. *Phys. Rev. B* **2005**, *71*, 235110.

(20) Karakus, M.; Jensen, S. A.; D'Angelo, F.; Turchinovich, D.; Bonn, M.; Cánovas, E. Phonon–Electron Scattering Limits Free Charge Mobility in Methylammonium Lead Iodide Perovskites. *J. Phys. Chem. Lett.* **2015**, *6*, 4991–4996.

(21) Huber, R.; Tauser, F.; Brodschelm, A.; Bichler, M.; Abstreiter, G.; Leitenstorfer, A. How Many-Particle Interactions Develop After Ultrafast Excitation of an Electron-Hole Plasma. *Nature* **2001**, *414*, 286–289.

(22) Valverde-Chávez, D. A.; Ponseca, C. S.; Stoumpos, C. C.; Yartsev, A.; Kanatzidis, M. G.; Sundström, V.; Cooke, D. G. Intrinsic Femtosecond Charge Generation Dynamics in Single Crystal $CH_3NH_3Pb_3$. *Energy Environ. Sci.* **2015**, *8*, 3700–3707.

(23) Lan, Y.; Dringoli, B. J.; Valverde-Chávez, D. A.; Ponseca, C. S.; Sutton, M.; He, Y.; Kanatzidis, M. G.; Cooke, D. G. Ultrafast Correlated Charge and Lattice Motion in a Hybrid Metal Halide Perovskite. *Sci. Adv.* **2019**, *5*, eaaw5558.

(24) Jung, J. W.; Williams, S. T.; Jen, A. K.-Y. Low-Temperature Processed High-Performance Flexible Perovskite Solar Cells Via Rationally Optimized Solvent Washing Treatments. *RSC Adv.* **2014**, *4*, 62971–62977.

(25) Yan, W.; Burgos-Caminal, A.; Das Gupta, T.; Moser, J.-E.; Sorin, F. Direct Synthesis of Selenium Nanowire Mesh on a Solid Substrate and Insights into Ultrafast Photocarrier Dynamics. *J. Phys. Chem. C* **2018**, *122*, 25134–25141.

(26) Burgos-Caminal, A.; Socie, E.; Bouduban, M. E. F.; Moser, J.-E. Exciton and Carrier Dynamics in Two-Dimensional Perovskites. *J. Phys. Chem. Lett.* **2020**, *11*, 7692–7701.

(27) Kim, K. Y.; Taylor, A. J.; Glownia, J. H.; Rodriguez, G. Coherent Control of Terahertz Supercontinuum Generation in Ultrafast Laser–Gas Interactions. *Nat. Photonics* **2008**, *2*, 605–609.

(28) Minami, Y.; Kurihara, T.; Yamaguchi, K.; Nakajima, M.; Suemoto, T. High-Power THz Wave Generation in Plasma Induced by Polarization Adjusted Two-Color Laser Pulses. *Appl. Phys. Lett.* **2013**, *102*, 041105.

(29) Karpowicz, N.; Dai, J.; Lu, X.; Chen, Y.; Yamaguchi, M.; Zhao, H.; Zhang, X.-C.; Zhang, L.; Zhang, C.; Price-Gallagher, M. et al. Coherent Heterodyne Time-Domain Spectrometry Covering the Entire "Terahertz Gap". *Appl. Phys. Lett.* **2008**, *92*, 011131.

(30) Lu, X.; Zhang, X.-C. Terahertz Wave Gas Photonics: Sensing with Gases. *J. Infrared Millim. Terahertz Waves* **2011**, *32*, 562–569.

(31) Dexheimer, S. L.; Baxter, J. B.; Schmuttenmaer, C. A. Time-Resolved Terahertz Spectroscopy and Terahertz Emission Spectroscopy. In *Terahertz Spectroscopy: Principles and Applications*; CRC Press, 2008.

(32) Dexheimer, S. L.; Kaindl, R. A.; Averitt, R. D. Time-Resolved Terahertz Studies of Carrier Dynamics in Semiconductors, Superconductors and Strongly Correlated Electron Materials. In *Terahertz Spectroscopy: Principles and Applications*; CRC Press, 2008.

(33) Ulbricht, R.; Hendry, E.; Shan, J.; Heinz, T. F.; Bonn, M. Carrier Dynamics in Semiconductors Studied with Time-Resolved Terahertz Spectroscopy. *Rev. Mod. Phys.* **2011**, *83*, 543–586.

(34) Richter, J. M.; Branchi, F.; Camargo, F. V. de A.; Zhao, B.; Friend, R. H.; Cerullo, G.; Deschler, F. Ultrafast Carrier Thermalization in Lead Iodide Perovskite Probed with Two-Dimensional Electronic Spectroscopy. *Nat. Commun.* **2017**, *8*, 376.

(35) March, S. A.; Riley, D. B.; Clegg, C.; Webber, D.; Liu, X.; Dobrowolska, M.; Furdyna, J. K.; Hill, I. G.; Hall, K. C. Four-Wave Mixing in Perovskite Photovoltaic Materials Reveals Long Dephasing Times and Weaker Many-Body Interactions than GaAs. *ACS Photonics* **2017**, *4*, 1515–1521.

(36) Beard, M. C.; Turner, G. M.; Schmuttenmaer, C. A. Transient Photoconductivity in GaAs as Measured by Time-Resolved Terahertz Spectroscopy. *Phys. Rev. B* **2000**, *62*, 15764–15777.

(37) Monti, M.; Tao, S. X.; Staniforth, M.; Crocker, A.; Griffin, E.; Wijesekara, A.; Hatton, R. A.; Lloyd-Hughes, J. Efficient Intraband Hot Carrier Relaxation in the Perovskite Semiconductor $Cs_{1-x}Rb_xSnI_3$ Mediated by Strong Electron–Phonon Coupling. *J. Phys. Chem. C* **2018**, *122*, 20669–20675.

(38) Kittel, C. *Introduction to Solid State Physics*, 5th ed.; John Wiley & Sons, Inc., 1976.

(39) Filip, M. R.; Verdi, C.; Giustino, F. GW Band Structures and Carrier Effective Masses of $CH_3NH_3PbI_3$ and Hypothetical Perovskites of the Type $APbI_3$: A = NH_4, PH_4, AsH_4, and SbH_4. *J. Phys. Chem. C* **2015**, *119*, 25209–25219.

(40) Even, J.; Pedesseau, L.; Katan, C.; Kepenekian, M.; Lauret, J.-S.; Sapori, D.; Deleporte, E. Solid-State Physics Perspective on Hybrid Perovskite Semiconductors. *J. Phys. Chem. C* **2015**, *119*, 10161–10177.

(41) Even, J.; Pedesseau, L.; Katan, C. Understanding Quantum Confinement of Charge Carriers in Layered 2D Hybrid Perovskites. *ChemPhysChem* **2014**, *15*, 3733–3741.

(42) Miyata, K.; Meggiolaro, D.; Trinh, M. T.; Joshi, P. P.; Mosconi, E.; Jones, S. C.; Angelis, F. D.; Zhu, X.-Y. Large Polarons in Lead Halide Perovskites. *Sci. Adv.* **2017**, *3*, e1701217.

(43) Cinquanta, E.; Meggiolaro, D.; Motti, S. G.; Gandini, M.; Alcocer, M. J. P.; Akkerman, Q. A.; Vozzi, C.; Manna, L.; De Angelis, F.; Petrozza, A. et al. Ultrafast THz Probe of Photoinduced Polarons in Lead-Halide Perovskites. *Phys. Rev. Lett.* **2019**, *122*, 166601.

(44) Yang, Y.; Ostrowski, D. P.; France, R. M.; Zhu, K.; van de Lagemaat, J.; Luther, J. M.; Beard, M. C. Observation of a Hot-Phonon Bottleneck in Lead-Iodide Perovskites. *Nat. Photonics* **2016**, *10*, 53–59.

(45) Niesner, D.; Zhu, H.; Miyata, K.; Joshi, P. P.; Evans, T. J. S.; Kudisch, B. J.; Trinh, M. T.; Marks, M.; Zhu, X.-Y. Persistent Energetic Electrons in Methylammonium Lead Iodide Perovskite Thin Films. *J. Am. Chem. Soc.* **2016**, *138*, 15717–15726.

(46) Zhu, H.; Miyata, K.; Fu, Y.; Wang, J.; Joshi, P. P.; Niesner, D.; Williams, K. W.; Jin, S.; Zhu, X.-Y. Screening in Crystalline Liquids Protects Energetic Carriers in Hybrid Perovskites. *Science* **2016**, *353*, 1409–1413.

(47) Zheng, F.; Wang, L. Large Polaron Formation and Its Effect on Electron Transport in Hybrid Perovskites. *Energy Environ. Sci.* **2019**, *12*, 1219–1230.

(48) Palmieri, T.; Baldini, E.; Steinhoff, A.; Akrap, A.; Kollár, M.; Horváth, E.; Forró, L.; Jahnke, F.; Chergui, M. Mahan Excitons in Room-Temperature Methylammonium Lead Bromide Perovskites. *Nat. Commun.* **2020**, *11*, 1–8.

TOC Graphic

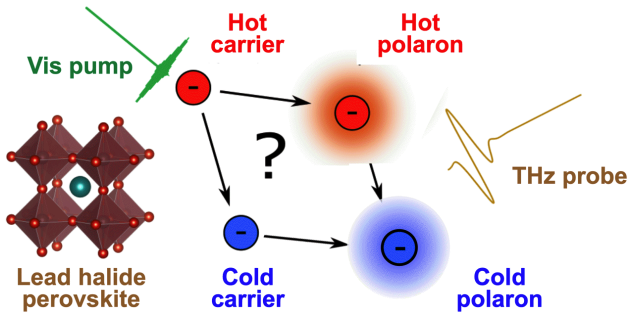
Hot
carrier
Hot
polaron
Vis pump
?
THz probe
Lead halide
perovskite
Cold
carrier
Cold
polaron

Hot Carrier Mobility Dynamics Unravel Competing Sub-ps Processes in Lead Halide Perovskites

Andrés Burgos-Caminal, Juan Manuel Moreno-Naranjo, Aurélien René Willauer, Arun Aby Paraecattil, Ahmad Ajdarzadeh, and Jacques-E. Moser *

Photochemical Dynamics Group, Institute of Chemical Sciences and Engineering, École Polytechnique Fédérale de Lausanne, 1015 Lausanne, Switzerland.

* Corresponding author. Email: je.moser@epfl.ch

Supporting Information

S1. Ultrabroadband THz pulses

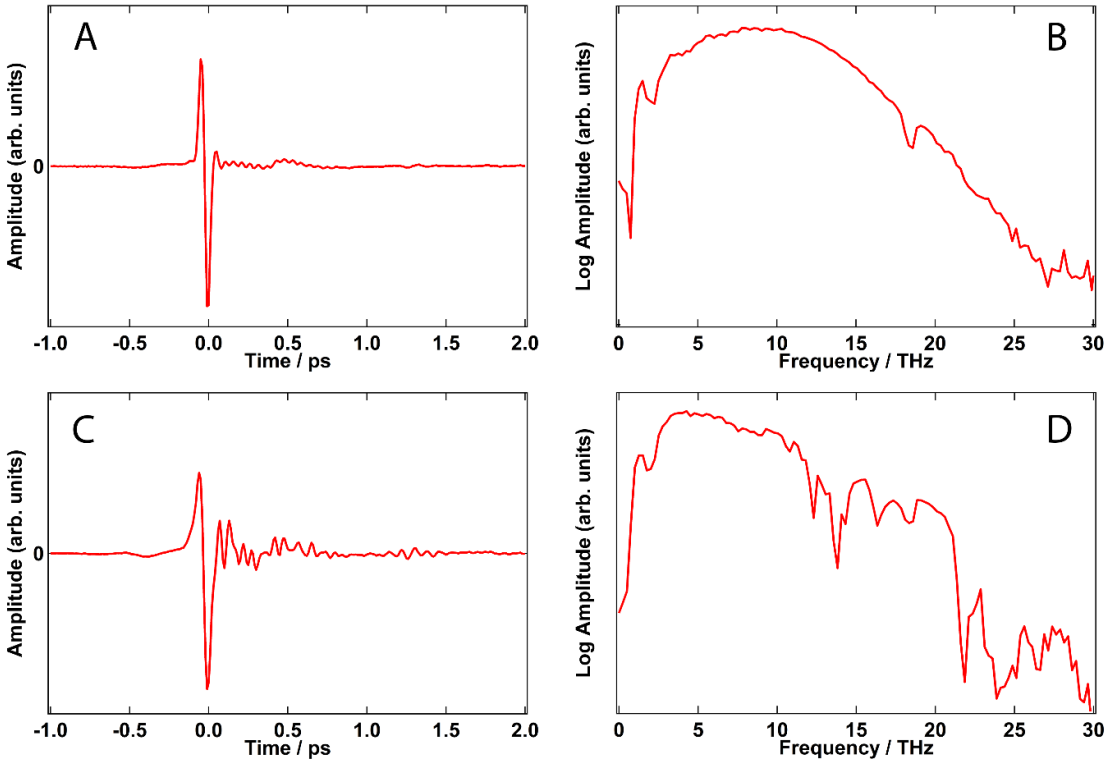

Figure S1. Typical pulse profiles obtained by ultrabroadband THz generation and analysis by plasma photonics as used in the present study. A) Temporal profile of the pulse detected in N_2. B) FT frequency profile obtained from the pulse shown in A. C) Temporal profile of the pulse detected in butane with TPX windows and D) its corresponding FT frequency profile. The observed dip at 18.5 THz corresponds to the phonon absorption band of the Si wafers used as filters.[1,2]

One of the main advantages of using an ultrabroadband TRTS spectrometer is the improved time resolution owing to the generation of shorter THz pulses. Measurements similar to those presented in this manuscript have previously been reported by Bretschneider *et al.*[3] However, those measurements were carried out with a classical spectrometer based on optical rectification in ZnTe crystals, where the obtained THz pulses have a duration ≥ 1 ps. This approach produces a considerable loss in time resolution, which can be easily observed when comparing the results with our own measurements. A clear difference can be observed by comparing the trace corresponding to an excitation wavelength of 760 nm, with no excess energy, presented in Fig. 1 of the present manuscript with that appearing in Fig. 2A of ref. [3]. While the former trace shows a fast rise with a time constant of ca. 200 fs, the latter trace displays a rise that takes up to 1 ps to complete. Both measurements were applied to $CH_3NH_3PbI_3$ films in similar conditions, and the difference cannot be explained in terms other than a difference in the time resolution due to the cross-correlation between the pump and probe pulses. As a result, the model fitted in the cited reference, with the parameters obtained, does not show any agreement with our data because it considers a slow exponential rise to be present, even when no excess energy is employed, which is a rise that we do not observe. Therefore, the reported rise must come from the difference between the widths of the instrument response function (IRF) employed in their model and the actual IRF of their data. Thus, this fact makes us doubt the validity of the conclusions obtained from their data analysis.

S2. Polymer substrate

When choosing a polymer to be used as a substrate in time-resolved terahertz spectroscopy (TRTS), minimization of the vibrational transitions that can produce strong absorption bands in the THz region is important. The first polymers to discard are those containing polar groups, such as poly(methyl methacrylate) (PMMA) or poly(ethylene terephthalate) (PET), or even any heteroatom, such as polytetrafluoroethylene (PTFE, Teflon™),[4] since they involve complete or partial absorption of the 1-20 THz spectrum, especially when using millimetre thick substrates. Therefore, we considered simple polymers, such as polypropylene (PP), polymethylpentene (PMP, TPX™), and high-density polyethylene (HDPE). In addition, branching (of a few carbon atoms) will generally lead to higher degrees of freedom and thus more vibrational modes to be excited. Indeed, HDPE, the simplest polymer, was found to be the most transparent up to a frequency of 20 THz and was chosen as the substrate to support lead halide perovskite (LHP) films in our experiments. TPX™ is an interesting material that can be used in windows for special applications in TRTS due to its transparency in both the THz region, up to 12 THz, and the visible region.

Thin films of LHPs composed of various anions and cations were obtained on 1 mm HDPE sheets through a spin-coating procedure, identical to that generally used on glass or similar supports. When spin-coating solutions to form LHP thin films, one of the key parameters, and the one that mainly varies between HDPE and glass, is the wettability of the surface to the polar solvent (DMSO). HDPE is an apolar material that repel polar solvents, making the spin-coating technique impracticable. Indeed, the spin-coating technique is based on the formation of a thin film of solution when a spinning force is applied. However, if poor interaction occurs between the solvent and the substrate, the solution just slips off. To solve this issue, a surface treatment must be applied to the HDPE surface to endow it with a polar nature. This nature was achieved through an oxidative plasma treatment. Such an

approach generates oxidation products on the surface of the polymer that constitute polar groups, highly increasing the wettability to polar solvents.[5] The resulting LHP films are polycrystalline and have photophysical properties similar to the films prepared on other substrates (Fig. S2).

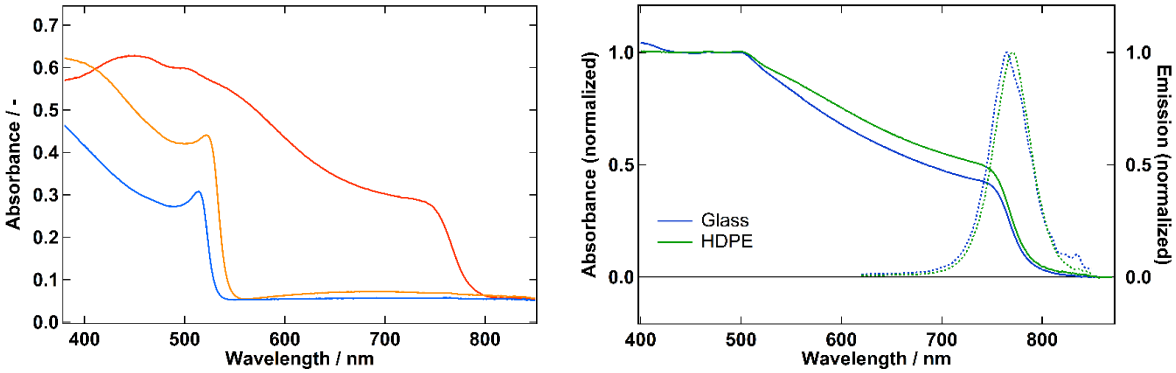

Figure S2. Left) Absorbance spectrum of thin films of $CH_3NH_3PbI_3$ (red), $CH_3NH_3PbBr_3$ (orange) and $CsPbBr_3$ (blue) spin-coated on a high-density polyethylene (HDPE) substrate. Right) Comparison of the absorbance and emission of a $CH_3NH_3PbI_3$ between using glass or HDPE as substrates.

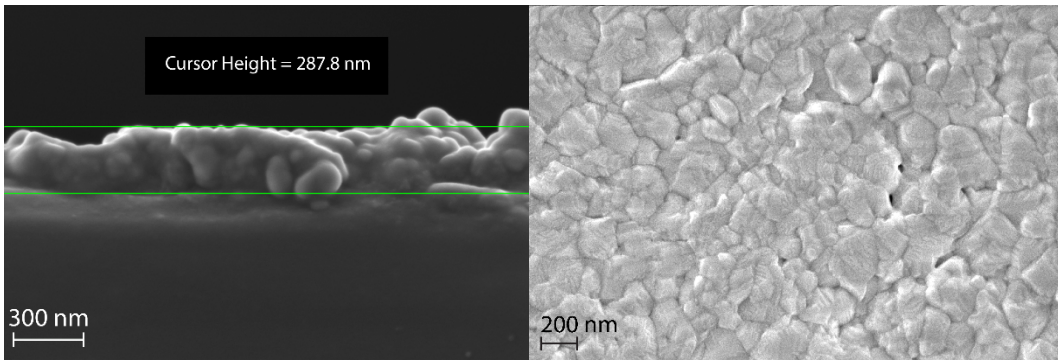

Figure S3. SEM cross-section (left) and surface (right) pictures of the $CH_3NH_3PbI_3$ film sample. The thickness of the perovskite layers is between 250 and 300 nm. The film is polycrystalline with some grains larger than 100 nm in diameter. The left picture is smoother due to a carbon coating treatment used in microscopy.

S3. Mathematical models

a) Simple model

As a first attempt, we can consider a simple model taking into account only hot and cold carriers, whose populations N_H and N_C, respectively, evolve according to:

$$\frac{\mathrm{d}N_H}{\mathrm{d}t} = -\frac{1}{\tau}\cdot N_H(t) \tag{S1}$$

$$\frac{\mathrm{d}N_C}{\mathrm{d}t} = \frac{1}{\tau}\cdot N_C(t) \tag{S2}$$

With the initial conditions are $N_H(0) = N^0{}_H(0)$ and $N_c(0) = N - N^0{}_H$, where N is the total density of carriers, we obtain:

$$N_H(t) = N_H^0\cdot\exp\left(\frac{-t}{\tau}\right) \tag{S3}$$

$$N_C(t) = 1 - N_H^0\cdot\exp\left(\frac{-t}{\tau}\right) \tag{S4}$$

The assumption that both hot and cold carriers will give a signal, albeit proportionally different to the concentration due to the different mobilities, is reasonable. Thus, for a normalized dataset, we can define the following model for the sample conductivity $S(t)$:

$$S(t) = 1 - \frac{N_H^0}{N}\cdot\exp\left(\frac{-t}{\tau}\right) + b\cdot\frac{N_H^0}{N}\cdot\exp\left(\frac{-t}{\tau}\right) \tag{S5}$$

where b is a proportionality constant due to the different mobilities (μ_H/μ_C). However, since the two exponentials are identical, b and $N^0{}_H/N$ cannot be determined individually through a fit, even if N is known. Only the product $B = (1-b)N^0{}_H/N$ can be determined. Thus, further simplification of the model is necessary, yielding a single exponential:

$$S(t) = 1 - B\cdot\exp\left(-\frac{t}{\tau}\right) \tag{S6}$$

If b or $N^0{}_H/N$ can be determined from a separate method, then the other parameter can be calculated. Otherwise, B is a measure of the difference in average mobility of the ensemble between the initial and final situation. If we assume in our model that μ_H and μ_C, and thus b, are constant, then, differences in B report different initial relative hot carrier densities ($N^0{}_H/N$), which lowers the initial average mobility. The values of B can range from 0 to 1. As the amount of initial hot carriers increases B will also increase. However, it will most likely never reach 1 since that would mean the initial average mobility is 0.

After convoluting the exponential equation (Eq. S6) with a Gaussian function of the form:

$$\frac{2}{w}\sqrt{\frac{\ln(2)}{\pi}}\cdot\exp\left(-\frac{4\ln(2)\cdot t^2}{w^2}\right) \tag{S7}$$

representing the cross-correlation of the pump laser and the THz probe pulses, and where *w* is the full width at half maximum (FWHM), we obtain the following equation to be fitted to the observed dynamics:

$$S(t)=\frac{1}{2}\left(1+\mathrm{erf}\left[2(t-t_0)\sqrt{\frac{1}{w^2}}\cdot\sqrt{\ln(2)}\right]-B\cdot\exp\left[\frac{w^2\left(1-\frac{16(t-t_0)\cdot\tau\cdot\ln(2)}{w^2}\right)}{16\,\tau^2\cdot\ln(2)}\right]\cdot\mathrm{erfc}\left[\frac{1-\frac{8(t-t_0)\cdot\tau\cdot\ln(2)}{w^2}}{4\mathrm{tc}\sqrt{\frac{1}{w^2}}\cdot\sqrt{\ln(2)}}\right]\right) \tag{S8}$$

b) <u>Competition model</u>

The competition model is obtained by numerically solving the below system of five differential equations (Eqs. S9-S13), where N_{hc}, N_{cc}, N_{loph}, N_{hp}, and N_{cp} correspond to the populations of the hot carriers, cold carriers, LO phonons, hot polarons, and cold polarons, respectively. The rate constants k_1, k_{-1}, k_2, k_3, and k_4 characterise the processes depicted in Scheme 2.

$$\frac{\mathrm{d}N_{hc}(t)}{\mathrm{d}t}=-k_1\cdot N_{hc}(t)+k_{-1}\cdot N_{cc}(t)\cdot N_{loph}(t)-k_2\cdot N_{hc}(t) \tag{S9}$$

$$\frac{\mathrm{d}N_{cc}(t)}{\mathrm{d}t}=k_1\cdot N_{hc}(t)-k_{-1}\cdot N_{cc}(t)\cdot N_{loph}(t)-k_2\cdot N_{cc}(t) \tag{S10}$$

$$\frac{\mathrm{d}N_{loph}(t)}{\mathrm{d}t}=k_1\cdot N_{hc}(t)-k_{-1}\cdot N_{cc}(t)\cdot N_{loph}(t)-k_3\cdot N_{loph}(t) \tag{S11}$$

$$\frac{\mathrm{d}N_{hp}(t)}{\mathrm{d}t}=k_2\cdot N_{hc}(t)-k_4\cdot N_{hp}(t) \tag{S12}$$

$$\frac{\mathrm{d}N_{cp}(t)}{\mathrm{d}t}=k_2\cdot N_{cc}(t)+k_4\cdot N_{hp}(t) \tag{S13}$$

The conductivity signal *S(t)* is finally approximated by considering that hot polarons, cold carriers, and cold polarons have the same mobility:

$$S(t)=N_{hp}(t)+a\cdot N_{hc}(t)+N_{cp}(t)+N_{cc}(t) \tag{S14}$$

where $N_{hp}(0)=0$ and $N_{cp}(0)=0$. Here, unlike in Scheme 2, the mobility is not considered to increase between hot and cold polarons as a simplification, since this process occurs outside the observed time window.

S4. Supplementary data and analysis

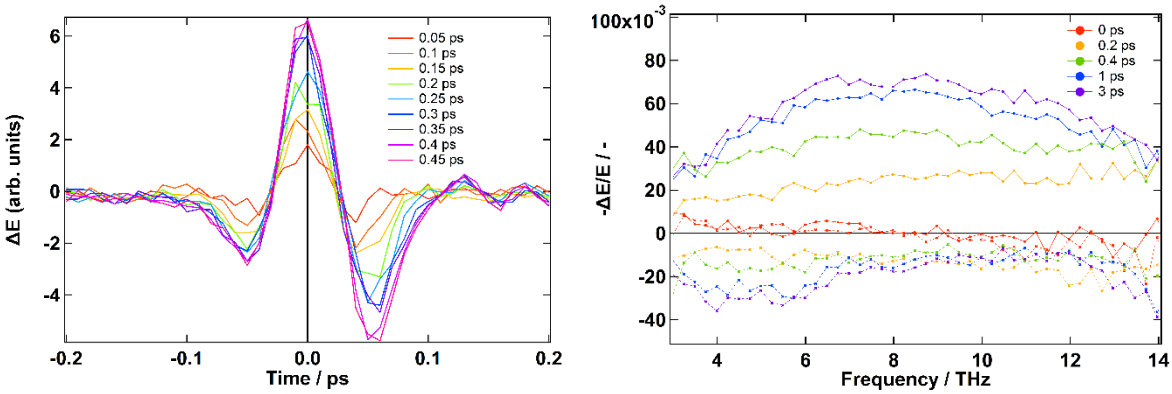

Figure S4. Time-resolved *ΔE(t)* (left) and *-ΔE(ω)/E(ω)* (right, Solid lines for Re and dashed for Im) obtained on $CH_3NH_3PbI_3$ at different pump-probe delay times (λ_{exc} = 510 nm, F = 62 µJ cm^{-2}). The changes can be assigned mainly to a change in amplitude and not a change in phase. This allows to follow the dynamics at this point.

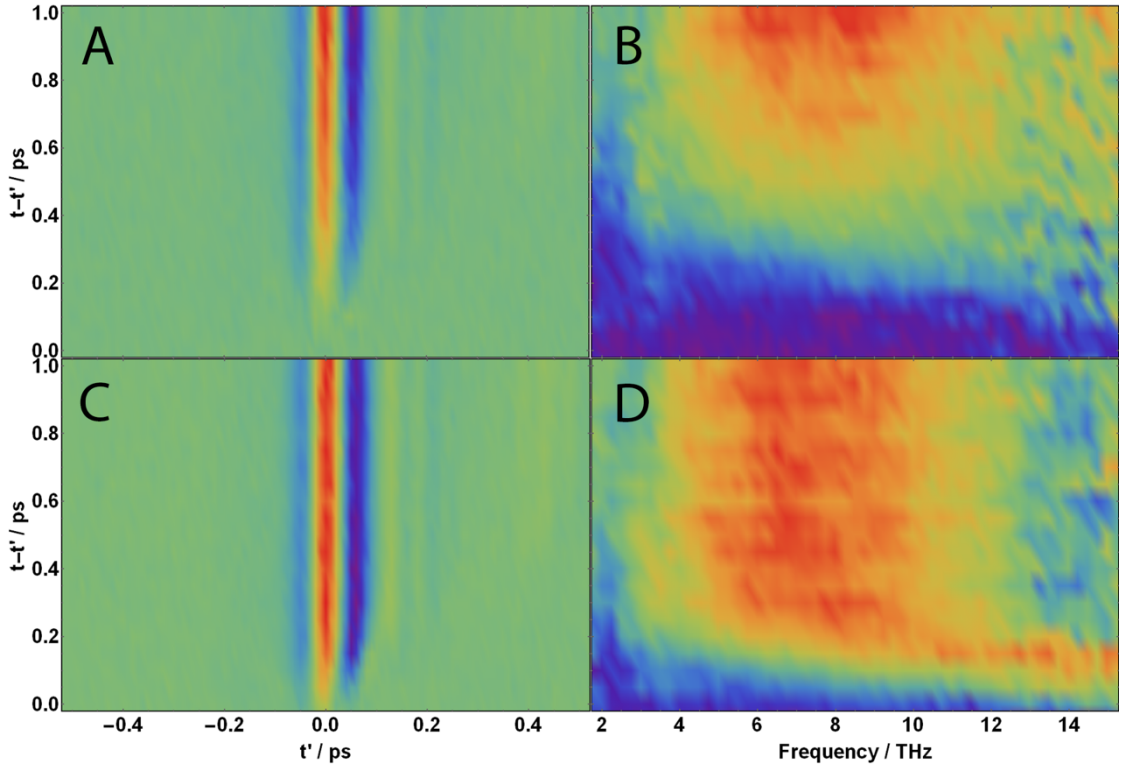

Figure S5. 2D maps of the first ps after photoexcitation at λ_{exc} = 510 nm (A, B) and λ_{exc} = 740 nm (C, D). A and C show the *ΔE(t)* waveform while B and D show the corresponding magnitude of the complex *-ΔE(ω)/E(ω)* spectra.

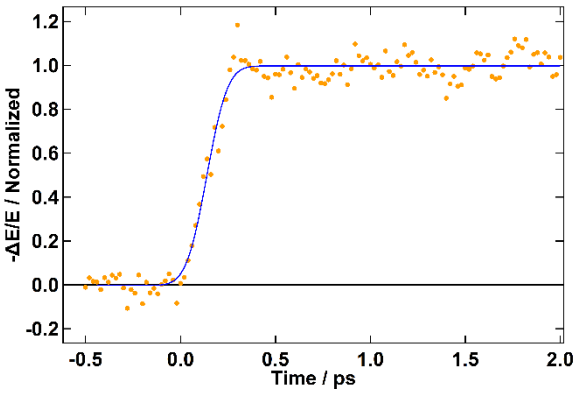

Figure S6. The rise of the photoconductivity on $CH_3NH_3PbI_3$ (λ_{exc} = 760 nm) can be well fitted to a very quick rise convoluted with a Gaussian of 200 fs in FWHM.

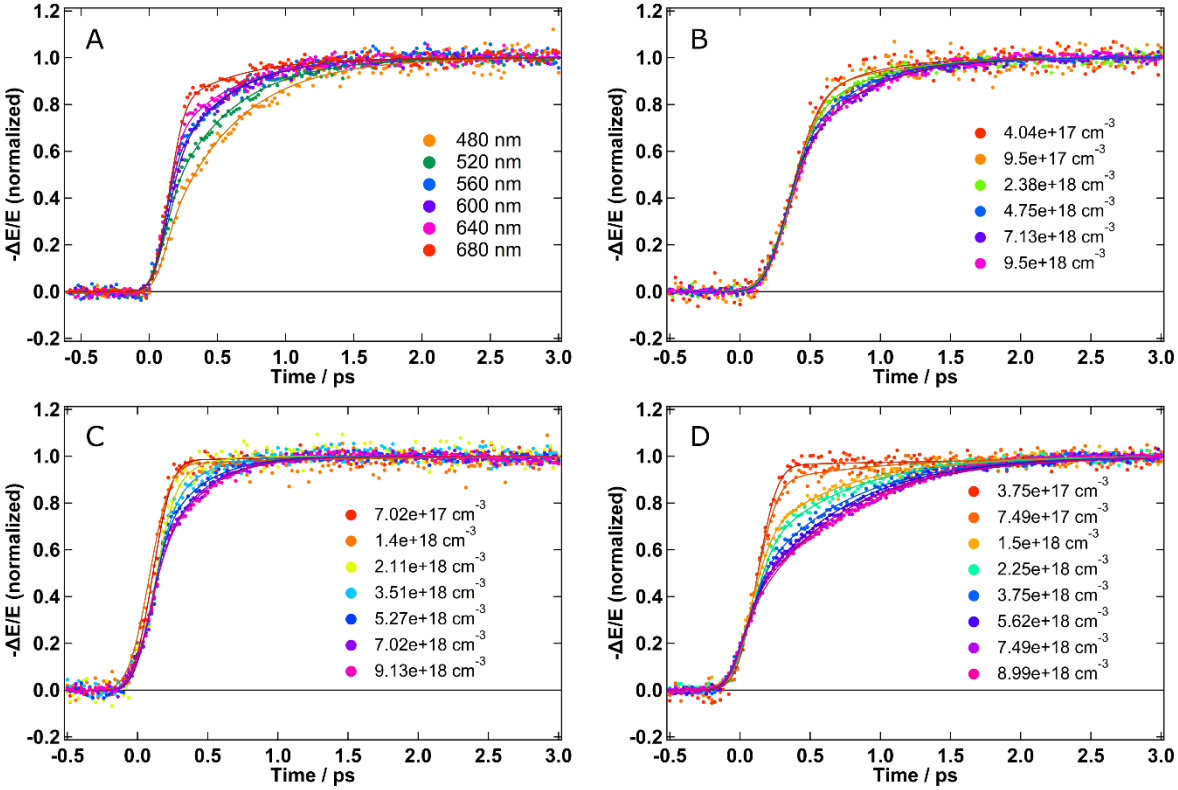

Figure S7. Fitting curves of the simple exponential model for $CH_3NH_3PbI_3$ (A and B), $CH_3NH_3PbBr_3$ (C) and $CsPbBr_3$ (D).

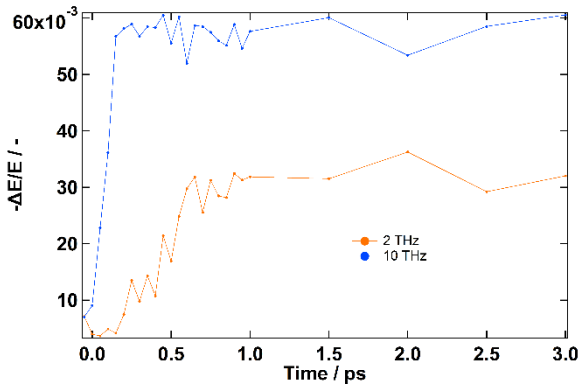

Figure S8. Delayed rise of the photoconductivity at 2 THz compared to that at 10 THz on $CH_3NH_3PbI_3$ (λ_{exc} = 740 nm).

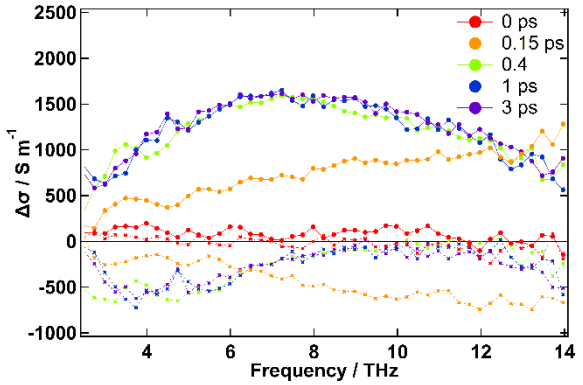

Figure S9. Change of the photoconductivity spectrum in the first hundreds of femtoseconds on $CH_3NH_3PbI_3$ (λ_{exc} = 740 nm, solid lines for Re and dashed for Im).

Drude-Smith analysis

Figure S10 shows photoconductivity spectra recorded at time delays ≤ 200 fs. Only at these early times the spectra follow a Drude-Smith behaviour, typical of free carriers in a nanocrystalline solid, as shown by the fit lines. Data fitting yields scattering time constants of τ = 2.8 fs and τ = 5.0 fs, as well as backscattering parameter values of c = – 0.89 and c = – 0.88, respectively. In the cold carrier case (λ_{exc} = 740 nm), we can calculate the carrier mobility as $\mu = (1+c)\, e\tau / m^*$. Using a reported effective mass in the order of $m^* = 0.2\ m_e$,[6] a value of μ = 5.3 $cm^2\ V^{-1}\ s^{-1}$ is obtained. This figure appears in the lower end of reported THz mobilities due to the strong backscattering component characterizing this type of LHP films.[6]

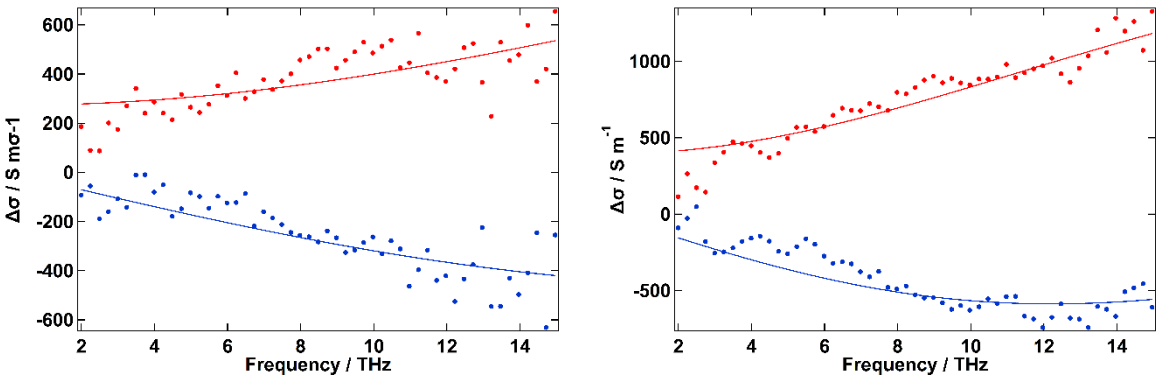

Figure S10. Photoconductivity spectra at very early times for λ_{exc} = 510 nm (left) and λ_{exc} = 740 nm (right) on $CH_3NH_3PbI_3$. The spectra correspond to Figs. S4 and S9 at time delays of 200 and 150 fs, respectively.

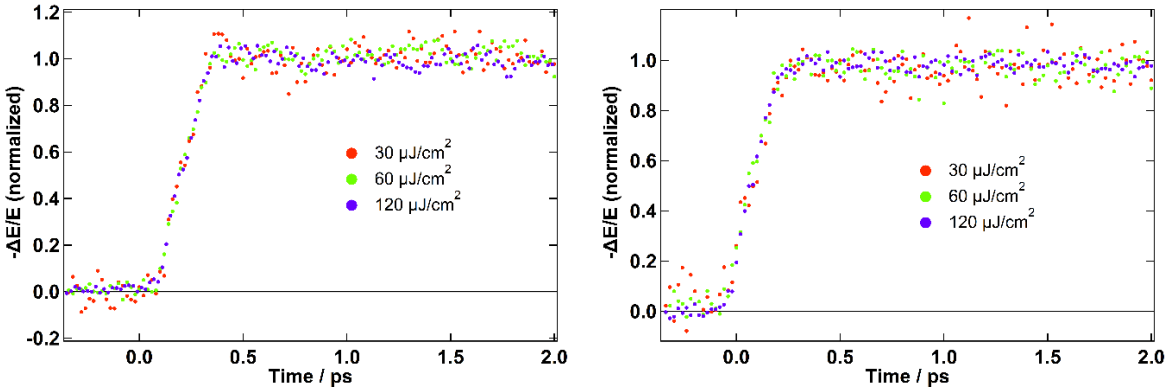

Figure S11. Fluence dependence of the THz absorptance signal at resonant excitation for $CH_3NH_3PbBr_3$ (λ_{exc} = 520 nm, left) and $CsPbBr_3$ (λ_{exc} = 510 nm, right). No dependence of the time evolution is observed.

Table S1. Results of the global fitting of the complex model to experimental data as seen in Fig. S11 for $CsPbBr_3$. The parameter *w* stands for the FWHM of the convoluted Gaussian, a measure of the time resolution of the setup. The initial hot carrier density $N_{hc}(0)$ is given in arbitrary density units (adu). The same units are used in the dimensions of the second order rate constant k_{-1}.

Parameter	*Fitted value*
a	0.15 ± 0.012
$N_{hc}(0)$	0.61 ± 0.03 adu
w	0.26 ± 0.004 ps
k_1	200 ps^{-1} (guessed)
k_{-1}	100 $adu^{-1}\,ps^{-1}$ (guessed)
$k_{-1} \cdot N_{hc}(0)$	61 ± 3 ps^{-1}
k_2	0.92 ± 0.018 ps^{-1}
k_3	1.67 ps^{-1} (literature)
k_4	0.01 ps^{-1} (literature)

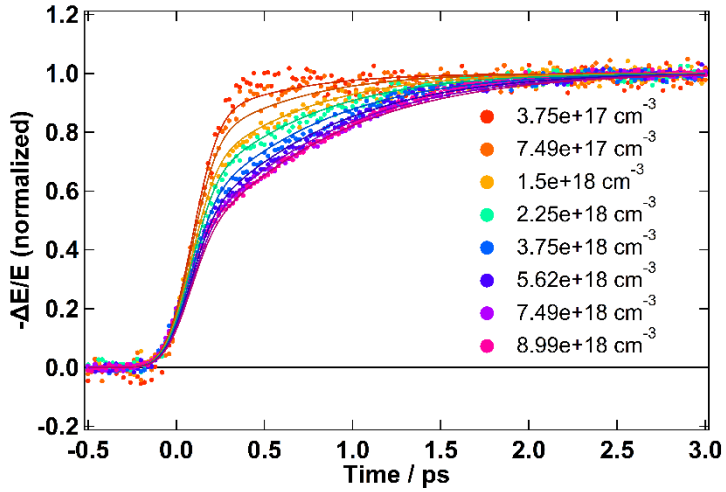

Figure S12. Model global fittings to $CsPbBr_3$ data, where all parameters are common and the initial carrier density is proportional to the fluence multiplied by a common fitted value.

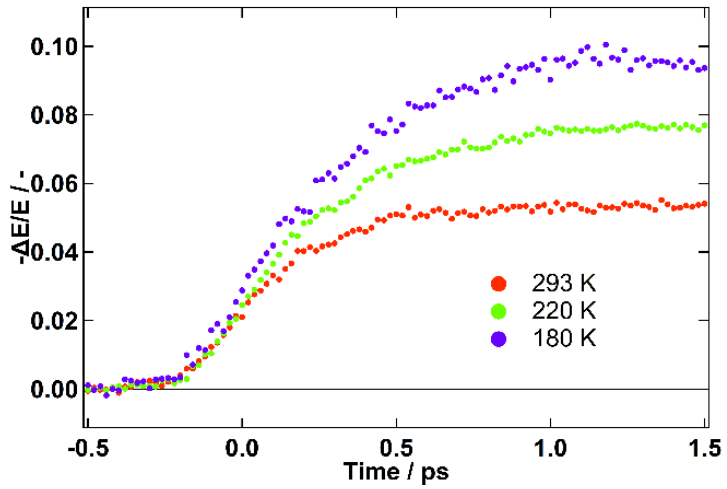

Figure S13. Low temperature measurements of the early dynamics of the THz absorptance in $CH_3NH_3PbBr_3$ (λ_{exc} = 400 nm).

References of the SI

(1) Johnson, F. A. Lattice Absorption Bands in Silicon. *Proc. Phys. Soc.* **1959**, *73*, 265–272.

(2) Karpowicz, N.; Dai, J.; Lu, X.; Chen, Y.; Yamaguchi, M.; Zhao, H.; Zhang, X.-C.; Zhang, L.; Zhang, C.; Price-Gallagher, M. et al. Coherent Heterodyne Time-Domain Spectrometry Covering the Entire "Terahertz Gap." *Appl. Phys. Lett.* **2008**, *92*, 011131.

(3) Bretschneider, S. A.; Ivanov, I.; Wang, H. I.; Miyata, K.; Zhu, X. Y.; Bonn, M. Quantifying Polaron Formation and Charge Carrier Cooling in Lead-Iodide Perovskites. *Adv. Mater.* **2018**, 1707312.

(4) D'Angelo, F.; Mics, Z.; Bonn, M.; Turchinovich, D. Ultra-Broadband THz Time-Domain Spectroscopy of Common Polymers Using THz Air Photonics. *Opt. Express* **2014**, *22*, 12475.

(5) Chai, J.; Lu, F.; Li, B.; Kwok, D. Y. Wettability Interpretation of Oxygen Plasma Modified Poly(Methyl Methacrylate). *Langmuir* **2004**, *20*, 10919–10927.

(6) Herz, L. M. Charge-Carrier Mobilities in Metal Halide Perovskites: Fundamental Mechanisms and Limits. *ACS Energy Lett.* **2017**, 1539–1548.